Available online at www.sciencedirect.com

SciVerse ScienceDirect

Ceramics International 39 (2013) 6877–6886

CERAMICS INTERNATIONAL

www.elsevier.com/locate/ceramint

# Room temperature elastic properties of gadolinia-doped ceria as a function of porosity

Xiaofeng Fan, Eldon D. Case*, Qing Yang, Jason D. Nicholas

*Chemical Engineering and Materials Science Department, Michigan State University, East Lansing, MI 48824, USA*

Received 25 January 2013; received in revised form 8 February 2013; accepted 9 February 2013
Available online 17 February 2013

**Abstract**

Gadolinia doped ceria (GDC) is commonly used in chemical reactors, gas sensors, gas separation membranes, and solid oxide fuel cells (SOFCs). In the present study, the room temperature elastic properties of GDC10 ($Ce_{0.9}Gd_{0.1}O_{1.95}$) were measured as a wide function of porosity for the first time. GDC10 specimens with volume fraction porosities ranging from 0.07 to 0.60 were produced by hard die pressing and sintering GDC10 powders in air at temperatures ranging from 825 to 1475 °C. The room temperature Young's modulus, shear modulus, bulk modulus and Poisson's ratio were measured using resonant ultrasound spectroscopy. The elastic moduli decreased exponentially with increasing porosity.


*Keywords:* B. Porosity; C. Mechanical properties; D. Ceria

## 1. Introduction

Dense gadolinia doped ceria (GDC) is commonly used as a membrane and/or diffusion blocking material in oxygen sensors, oxygen separators, and solid oxide fuel cells (SOFCs) [1–3]. In contrast, porous GDC is commonly used as an anode catalyst [4,5], an anode mixed ionic electronic conductor (MIEC) [6], an oxygen storage material [5], a mechanical support [7], and/or a composite cathode oxygen ion conductor [8] within these same devices. In fact, nano-composite cathodes (NCC's) of porous GDC surface-decorated with nano-sized MIEC catalyst particles have received much attention in the literature due to their high electrochemical performance [9–13] and electrochemical/microstructural durability [14] at intermediate (500–700 °C) temperatures. Like conventional SOFCs, SOFCs utilizing NCC's [15,16] must be designed so that coefficient of thermal expansion (CTE) mismatch between the cell layers (electrolyte, cathode, current collector, etc.) do not lead to fracture [17–19]. Unfortunately, the porous GDC elastic properties needed to model load transfer into the MIEC–GDC NCC layer are not available in the literature (to a first order approximation, the mechanical response of a NCC is determined solely by that of the porous, structurally-supporting, ionic-conducting scaffold).

The mechanical property literature for SOFC materials has been almost entirely limited to materials with relatively low porosity. For example, hardness and fracture toughness have been measured for samaria-doped ceria [20] and gadolina-doped ceria [21,22] but only for specimens with $P < 0.08$. In terms of the fracture strength, $\sigma_f$, of GDC10 ($Ce_{0.9}Gd_{0.1}O_{1.95}$) in particular, the values available in the literature also include only low porosity specimens, with $\sigma_f$ values from 200 to 300 MPa ($P < 0.08$) [23] and from 150 to 175 MPa ($P < 0.04$) [24]. While no creep data for GDC10 is available in the literature, Ikuma et al. studied the creep of undoped ceria with $0.01 < P < 0.08$ [25]. Two recent reviews of the mechanical properties of SOFC materials by Nakajo et al. [26,27] included creep data on SOFC materials other than GDC, but no creep data on GDC. Routbort et al. [28] studied GDC creep above 1200 °C, but only for samples with $P < 0.08$. In addition, Nakajo et al. [26] noted that creep data was extremely sparse for any porous SOFC material but suggested that finite element models that deal with the deformation of struts can perhaps be "adequate for preliminary studies,

*Corresponding author. Tel.: +1 517 353 6715; fax: +1 517 432 1105.
*E-mail address:* casee@egr.msu.edu (E.D. Case).

0272-8842/$ - see front matter © 2013 Elsevier Ltd and Techna Group S.r.l. All rights reserved.
http://dx.doi.org/10.1016/j.ceramint.2013.02.022

because of the actual uncertainties on the creep behavior of SOFC materials''. Lastly, as will be discussed in detail in Section, 3.2, the available literature data on elastic modulus and Poisson's ratio of GDC10 includes only low porosity specimens. Therefore, the present paper focuses on the room temperature elastic moduli and Poisson's ratio of GDC10 over a wide range of porosity ($0.07 \leq P \leq 0.60$).

## 2. Experimental methods

### 2.1. Specimen preparation

All GDC10 specimens were prepared from a single batch of 99.9% pure, 30.7 $m^2/g$ (~27 nm primary particle size) Anan Kasei $Ce_{0.9}Gd_{0.1}O_{1.95}$ (GDC10) powder obtained from Rhodia, Inc. (Cranbury, NJ). Light scattering measurements performed by the vendor yielded a 240 nm $d_{50}$ (i.e. the diameter of particle agglomerates in the 50th volumetric percentile) particle size. This value was consistent with previous transmission electron microscopy, x-ray diffraction, and light scattering measurements on a separate lot of 30–35 $m^2/g$ Rhodia GDC10 powder [29] which showed ~30 nm equiaxed primary particles grains agglomerated into lenticular masses 75 nm wide and 600 nm long. Vendor analysis on this previous lot of GDC10 powder showed it to have less than 10 ppm $SiO_2$ [29]. All powder processing in the present study was done in the absence of Pyrex® glassware and other potential sources of Si contamination.

Cylindrical specimens $2.7 \pm 0.3$ g in weight were prepared for mechanical testing by cold pressing the GDC10 nano-powders to 27.3 MPa in a $^3/_4''$ stainless steel die. These specimens were fired in air with a 4 °C/min heating rate and held for 5 h at various temperatures in order to produce specimens of varying porosities.

### 2.2. Elastic modulus measurements

The resonant ultrasound spectroscopy (RUS) technique [30,31] was used to measure the elastic moduli of as-sintered GDC10 specimens which were fired to 825, 850, 875, 900, 950, 975, 1000, 1050, 1100, 1200, 1450, or 1475 °C and therefore had sintered porosities of 60, 55, 48, 45, 38, 33, 27, 23, 15, 18, 8 and 6%, respectively. RUS is a non-destructive technique that has been used to measure the elastic moduli for a number of different oxides including hydroxyapatite [32,33], alumina [33] and lithium lanthanum zirconia oxide [34] as well as non-oxide ceramics [35], thermoelectrics [36,37], metals [38,39] and composites [40,41].

The RUS equipment (RUSpec, Quasar International, Albuquerque, NM) used in the present study consists of a computer controlled transceiver and a tripod arrangement of PZT (lead zirconate titanate) transducers that includes a single driver transducer and two pick-up transducers. Each specimen was placed on the tripod transducer stage where the driver transducer excited the mechanical vibrations in the specimen and the other two transducers detected the acoustic response of the specimen. The frequency of the driver transducer was swept from 10 kHz to 500 kHz in 29,999 steps. The resonant vibrational frequencies of the specimen were sensed and recorded (Fig. 1). Using the frequencies of the resonant peaks (Fig. 1) along with the specimen mass and dimensions, the elastic moduli of the disc-shaped specimens were calculated using a commercial software package (CylModel, Quasar International, Albuquerque, NM).

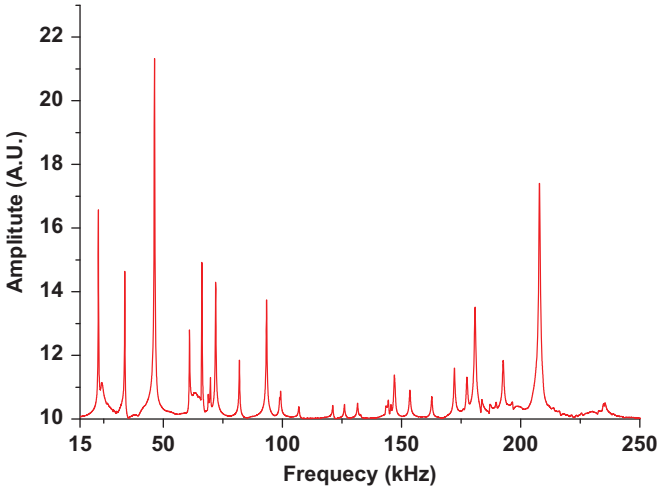


Fig. 1. A portion of the RUS spectrum obtained for GDC10 specimen with $P=0.52$ in the present study (A.U. stands for arbitrary units).

### 2.3. Microstructural examination procedures

An Auriga Dual Column focused ion beam-scanning electron microscope (FIB-SEM) (Carl Zeiss Microscopy, LLC, Thornwood, NY) with a nominal $x$–$y$ resolution of 1 nm was used to perform microstructural examinations on four fractured surfaces and one thermally etched polished surface. The thermally etched specimen was prepared by polishing down specimen ♯5 ($P=0.077$) to a final grit of 1 μm and holding the specimen in air for 2 h at 1350 °C (1350 °C is 100 °C lower than the 1450 °C sintering temperature used to produce this specimen). In order to suppress electrostatic charging during SEM analysis, a 15 nm thick gold coating was sputtered onto all specimen surfaces prior to SEM examination. The mean grain size was evaluated from the SEM micrographs via the linear intercept technique using a total of 150–200 intercepts per micrograph with a stereographic projection factor of 1.5 [42].

## 3. Results and discussion

### 3.1. Microstructural analysis

For the GDC10 specimens included in the present study, the evolution of the microstructure as a function of $P$ is depicted in Fig. 2. For $P=0.521$(specimen ♯39, Fig. 2a),

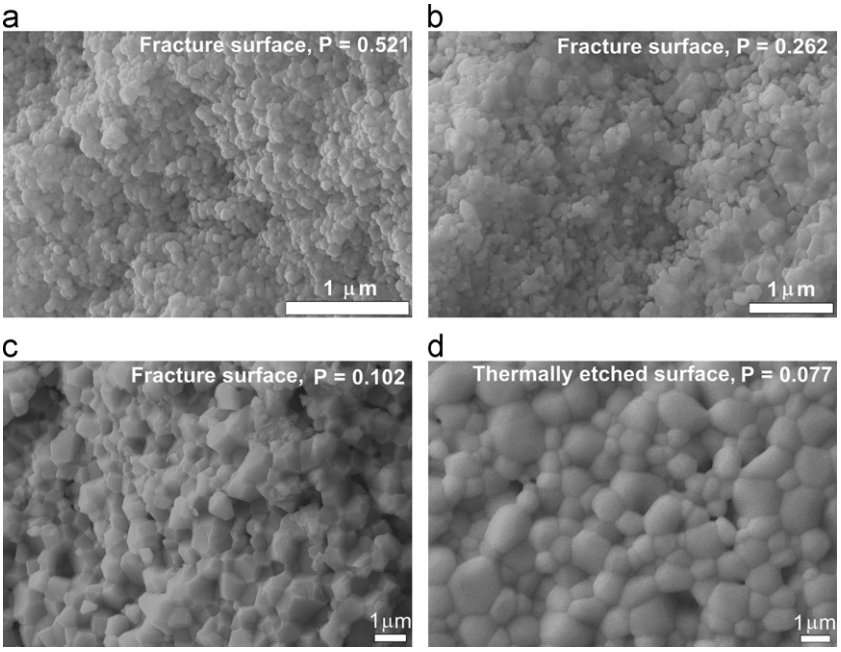


Fig. 2. SEM micrographs of (a) fracture surface for GDC10 specimen ♯39 ($P$=0.521); (b) fracture surface for GDC10 specimen ♯11 (P=0.262); (c) fracture surface for GDC10 specimen ♯3 ($P$=0.102) and (d) thermally etched polished surface for GDC10 specimen ♯5 ($P$=0.077).

clusters of agglomerates appear with aspect ratios of roughly 1.1–1.7 and agglomerate dimensions of ~350 nm × ~200 nm to ~150 nm × ~100 nm. For $P$=0.262 (specimen ♯11, Fig. 2b), relatively dense islands of grains with tubular pores along the grain boundaries are separated by relatively porous regions. For $P$=0.102 (specimen ♯3, Fig. 2c) and $P$=0.177 (specimen ♯14, micrograph not shown), the fracture mode is predominately intergranular. These more dense microstructures are more uniform, with pores ranging from several to hundreds of nanometers across located at triple points. For $P$=0.077 (specimen ♯5, Fig. 2d), this thermally etched specimen shows equiaxed grains and isolated pores of up to hundreds of nanometers across located at triple points or grain boundaries.

A grain-size density trajectory for the GDC10 specimens in the present study is typical of that observed for a variety of oxide ceramics [43,44], namely there is limited grain growth from green density up to relative density, RD, of roughly 0.8–0.85 (corresponding to a volume fraction porosity of ~0.2–0.15). For RD > 0.8, the grain size of the GDC10 specimens increased rapidly from about 0.3 μm to 1.1 μm for RD = 0.93 ($P$ = 0.07, Figs. 2d and 3). This implies that approximately two thirds of the 21 GDC10 specimens included in the present study had grain sizes from roughly 0.1 μm to 0.3 μm (Fig. 3).

The grain-size density trajectory (Fig. 3) for the GDC10 specimens was least-squares fit to the following empirical relationship:

$$GS = A_1 \exp\left(\frac{RD}{B_1}\right) + GS_0 \quad (1)$$

where $A_1$ and $B_1$ define the shape of the exponential curve. $A_1$ has units of grain dimension, $B_1$ is dimensionless and

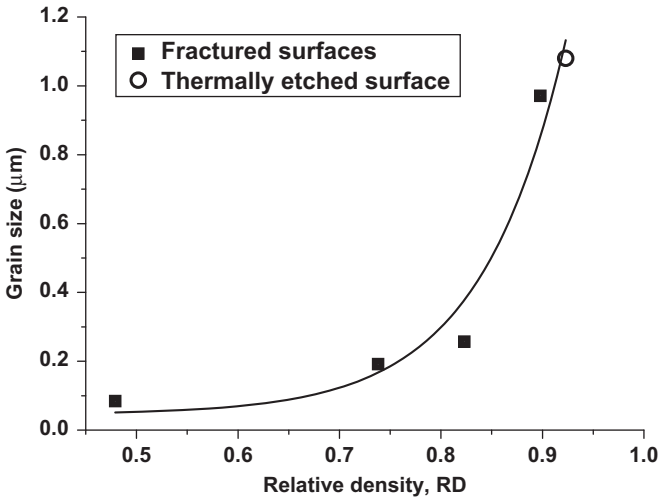


Fig. 3. Grain size-density trajectory for the GDC10 specimens in the present study. The solid curves represents the least-squares fit of the grain size versus density data to Eq. (1).

$GS_0$ is the initial powder particle size. The least-squares fit of the grain size versus relative density data to Eq. (1) gives $A_1$ = 0.00002 μm, $B_1$ = 0.085 and $GS_0$ = 0.046 μm, with a coefficient of determination, $R^2$ = 0.963. Eq. (1) describes the grain size-density trajectory very well for the GDC10 specimens included in the present study as well as a grain size-density trajectory from the literature for sintered hydroxyapatite [43]. Taken together, these results represent the first time detailed microstructural analyses of GDC10 grain size, pore shape, fracture mode, and porosity have been reported along with elastic property measurements.

### 3.2. Elastic modulus as a function of porosity

Several studies in the literature report on the elastic moduli of relatively dense bulk GDC10 specimens [45–48]. Among these studies [45–48], only Selcuk and Atkinson [45] report the Young's modulus as a function of volume fraction porosity, $P$. Using the impulse excitation technique (IET), Selcuk and Atkinson [45] measured the Young's modulus, $E$, shear modulus, $G$, and Poisson's ratio, $v$, for 26 disc-shaped polycrystalline GDC10 specimens over a very limited $P$ range, namely $0.02 < P < 0.05$ (Table 1). (The number of specimens was not directly stated by Selcuk and Atkinson [45] but here 26 data points have been extracted from Selcuk and Atkinson's plots). The Amezawa et al. [46] and Kushi et al. [47] GDC10 elasticity measurements were performed using the sonic resonance technique in a low $pO_2$ atmosphere (Table 1). As will be discussed later in this section, heating in a low $pO_2$ atmosphere can induce atomic scale defects which can in turn decrease the elastic modulus [48,49]. Wang et al.'s E data [48] was obtained by nano-indentation on $a > 98\%$ dense GDC10 specimen cooled from 800 °C and various $pO_2$ levels (Table 1).

In the present study, the RUS technique was employed to measure the $E$, $G$, $v$ and the bulk modulus, $B$, for 21 disk-shaped, as-sintered GDC10 specimens with $P$ values ranging from 0.07 to 0.60, where the porosity of the green (unfired) powder compacts, $P_G$, was 0.62. The porosity dependence of $E$, $G$ and $B$, was assumed to have the same functional forms (Eqs. (2)–(5)) employed by Selcuk and Atkinson [45], namely

$$M = M_0 \exp(-b_M P) \tag{2}$$

$$M = M_0(1-b_M P) \tag{3}$$

$$M = M_0\left[1+\frac{b_M P}{1-(b_M+1)P}\right] \tag{4}$$

$$M = M_0(1-P)^2(1+b_M P) \tag{5}$$

where $M$ represents the elastic moduli ($E$, $G$, or $B$ in this case), $M_0$ is the elastic moduli at $P=0$ and $b_M$ is a unit less, material-dependent constant that measures the rate of decrease in $M$ with increasing $P$. For $P \to 0$, Eqs. (2), (4) and (5) are approximated well by the linear relationship given by Eq. (3). Eq. (2) is an empirical relationship widely used to describe the elastic modulus change as a function of porosity [50]. Eq. (4) is modified from Eq. (2) to treat materials with dilute distribution of spherical pores [51]. Eq. (5) is based on the theoretical composite sphere model, where spherical pores were treated as a second phase randomly distributed in the matrix material [52].

Eqs. (2)–(5) were used to fit the Young's modulus for GDC10 specimens in the present study. Among Eqs. (2)–(5), the exponential relationship (Eq. (2)) best described the E versus P data. Since Eqs. (3)–(5) are best suited to low porosity, $P$, and the exponential relationship (Eq. (2)) is approximated by the linear form (Eq. (3)), it is not surprising that Eqs. (2)–(5) fit the Selcuk and Atkinson elasticity data (for which $0.02 < P < 0.5$) about equally well (Table 2). For Eqs. (2)–(5), Table 2 compares the least-squares fitting parameters and $R^2$ for (i) the data from the present study, (ii) the Selcuk and Atkinson data [45] and (iii) the combined data set (the present study, and references [45–47]). When $E$ data from the present study and the combined data set are least-squares fit to Eqs. (2)–(5), then based on the $R^2$ values in Table 2, Eq. (2) provides the best description of the $P$ dependence of the Young's, shear and bulk moduli (Table 2). Also, the values of $E_0$ predicted by Eqs. (3) and (5) are lower than all of the 26 points in the Selcuk and Atkinson study (Fig. 4), thus, the $E_0$ values from Eqs. (3) and (5) are not physically reasonable. Also, the $E_0$ value of 292 GPa predicted by Eq. (4) seems unreasonably high (Fig. 4). In contrast, the $E_0$ value predicted by Eq. (2) fits well the $E$ versus $P$ trend (Fig. 4).

The $E_0$ and $R^2$ values provided by Selcuk and Atkinson [45] were similar for each equation (Eqs. (2)–(5)). However,

Table 1
Comparison of specimen fabrication techniques, elastic modulus measurement techniques and porosity ranges for the present study, Selcuk and Atkinson [45], Amezawa et al. [46], Kushi et al. [47] and Wang et al. [48].

| References | Specimen fabrication technique | Elastic modulus measurement technique | Relative porosity range |
|---|---|---|---|
| The present study | Hard die pressed at 27.3 MPa, sintered from 825 °C to 1450 °C for 5 h | Resonant ultrasound spectroscopy | 0.066–0.595 |
| Selcuk and Atkinson [45] | Circular disk cut from extruded green tape, binder burn out at 400 °C, densified at 1500 °C for 1 h | Impulse excitation technique | 0.02–0.05 |
| Amezawa et al. [46] | Powder prepared by co-precipitation, hydrostatically pressed at 150 MPa, sintered at 1550 °C for 5 h | Sonic resonance measurement. Room temperature, one specimen under 0.01% $O_2$, one under 99.15% $H_2$ and 0.85% $H_2O$ | 0.035 and 0.033 |
| Kushi et al. [47] | Powder prepared by co-precipitation, hydrostatically pressed at 150 MPa, sintered at 1550 °C | Sonic resonance measurement. Room temperature under pure Argon | 0.051 |
| Wang et al. [48] | Powder mixed with 3 wt% PVB, uniaxially pressed then CIPed at 250 MPa. Held at 400 °C for 1 h and sintered at 1550 °C for 20 h | Nanoindentation, with assumed Poisson's ratio of 0.3 | $< 0.02$ |

Table 2
Fitting parameters, $E_0$ and $R^2$, for the least-squares fit of Young's modulus data for the present study, Selcuk and Atkinson [45], and the combined data set (the present study, [45–47]) to Eqs. (2)–(5).

| Reference | $E_0$ from Eq. (2) (GPa) | $E_0$ from Eq. (3) (GPa) | $E_0$ from Eq. (4) (GPa) | $E_0$ from Eq. (5) (GPa) | $R^2$ from Eq. (2) | $R^2$ from Eq. (3) | $R^2$ from Eq. (4) | $R^2$ from Eq. (5) |
|---|---|---|---|---|---|---|---|---|
| The present study | 235.2 | 161.3 | 292.0 | 175.7 | 0.989 | 0.931 | 0.969 | 0.963 |
| Selcuk and Atkinson [45] | 217.8[a] | 218.1[a] | 217.0[a] | 218.5[a] | 0.886[a] | 0.886[a] | 0.885[a] | 0.885[a] |
| Combined data set (the present study, [45–47]) | 226.7 | 200.3 | 239.8 | 206.4 | 0.992 | 0.942 | 0.987 | 0.986 |

[a] $E_0$ and $R^2$ values are taken from Selcuk and Atkinson [45].

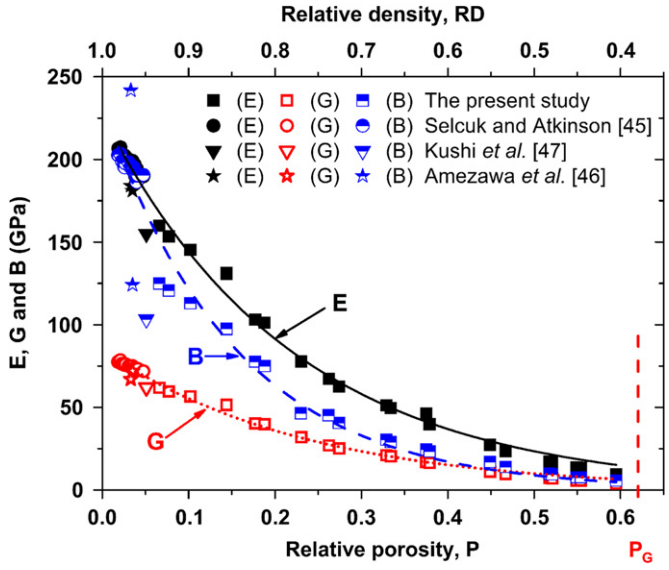


Fig. 4. Young's modulus, shear modulus and bulk modulus versus porosity for GDC10 specimens from the combined data set (the present study, Selcuk and Atkinson [45], Amezawa et al. [46], and Kushi et al. [47]). The solid, dashed and dotted curves represent the least-squares fit to Eq. (2) for the $E$–$P$, $B$–$P$ and $G$–$P$ data, respectively.

the $R^2$ values were lower than the present study or the combined data set (the present study, and references [45–47]). The lower $R^2$ values for the Selcuk and Atkinson study [45] may be related to the small porosity range (0.02–0.05) in that study, thus a small error in the measured porosity, $P$, can lead to a large relative error in the ($E$, $P$) data values.

Eq. (2) was also used to fit the $E$, $G$ and $B$ values for the combined data set (with data from the present study, and references [45–47]) (Fig. 4). Although Selcuk and Atkinson [45], Amezawa et al. [46] and Kushi et al. [47] did not report $B$ values in their studies, for isotropic polycrystalline specimens, $B$ can be calculated from the $E$ and $G$ data supplied by Selcuk and Atkinson [45], Amezawa et al. [46] and Kushi et al. [47] using Eq. (6), which allowed $E$, $G$, and $B$ to be plotted for the combined data set (Fig. 4).

$$B = \frac{EG}{3(3G-E)} \tag{6}$$

The least-squares fit parameters obtained for the 50 pairs of modulus-porosity data points for $E$, $G$ and $B$ from the combined dataset (the present study, and references [45–47])) to Eq. (2) are $E_0 = 226.7 \pm 4.4$ GPa, $b_E = 4.5 \pm 0.2$; $G_0 = 85.0 \pm 0.7$ GPa, $b_G = 4.3 \pm 0.1$; $B_0 = 233.7 \pm 6.6$ GPa, $b_B = 6.5 \pm 0.5$. The coefficients of determination, $R^2$, were 0.992, 0.993 and 0.950 for $E$, $G$ and $B$, respectively (Table 3). $E_0$, $G_0$ and $B_0$ (the extrapolations of the $E$, $G$ and $B$ data to $P=0$) obtained from the least-squares fit are useful in that they can be compared directly to the aggregated average moduli from single crystal data [53] or the theoretical elastic moduli values calculated from the density functional theory [54] or the statistical moment method [55].

Except for the Young's modulus measured by nano-indentation [48], the moduli obtained from the three different experimental techniques: RUS (the present study), sonic resonance [46,47] and IET [45] agree extremely well, even accounting for a possible shift in modulus due to low $pO_2$ for GDC10 from the Amezawa et al. [46] and Kushi et al. [47] studies. In general, a low $pO_2$ induces atomic scale defects (mainly oxygen vacancies) which in turn lower the observed elastic moduli in GDC10 specimens [46,47,56] and 7 wt% yttria stabilized zirconia [57].

Wang et al. [58] computed the $E$ value from their nano-indentation data using the Oliver–Pharr equation [59], such that

$$\frac{1}{E_r} = \frac{(1-\upsilon^2_{\text{indenter}})}{E_{\text{indenter}}} + \frac{(1-\upsilon^2_{\text{sample}})}{E_{\text{sample}}} \tag{7}$$

where $E_r$ is the reduced modulus, which is functions of both the modulus of the indenter and the specimen. $\upsilon_{\text{indenter}}$ and $\upsilon_{\text{sample}}$ are the Poisson's ratios of the diamond indenter and the specimen, respectively. $E_{\text{indenter}}$ and $E_{\text{sample}}$ are the elastic modulus of the diamond indenter and the specimen, respectively. Assuming $\upsilon_{\text{indenter}} = 0.07$, $E_{\text{indenter}} = 1140$ GPa for the diamond indenter and $\upsilon_{\text{sample}} = 0.3$, the $E$ value for 98% dense GDC10 [48] is 254.6 GPa. Several research groups have noted differences between the elastic moduli obtained via nano-indentation and the elastic moduli measured by dynamic methods such as RUS, sonic resonance and IET. For example, in a study by Radovic et al. [60] that compared $E$ measurements by the nano-indentation and RUS techniques, the $E$ values measured by nano-indentation were 10% higher than $E$ measured by RUS. Similarly, for skutterudite thermoelectric materials, Schmidt et al. [61] reported that $E$ measured via nano-indentation was 8% higher than $E$ measured by RUS.

While Eq. (2) fits the elastic modulus versus $P$ data relatively well, it has been observed empirically that the fit

Table 3
The number of data points, ND, parameters from least-squares fit to Eq. (2), $E_0$, $b_E$, $G_0$, $b_G$, $B_0$, $b_B$, and coefficient of determination, $R^2(E)$, $R^2(G)$ and $R^2(B)$. $E_0$, $G_0$ and $B_0$ are intercepts of the least-squares fits with the $y$-axis, respectively.

| Reference | ND | $E_0$ (GPa) | $b_E$ | $R^2$ ($E$) | $G_0$ (GPa) | $b_G$ | $R^2$ ($G$) | $B_0$ (GPa) | $b_B$ | $R^2$ ($B$) | Relative porosity range |
|---|---|---|---|---|---|---|---|---|---|---|---|
| The present study | 21 | 235.2 | 4.7 | 0.989 | 88.4 | 4.5 | 0.987 | 190.7 | 5.4 | 0.986 | 0.07–0.60 |
| Selcuk and Atkinson [45] | 26 | 217.8 | 2.9 | 0.886 | 82.2 | 3.0 | 0.871 | 211.1 | 2.5 | 0.788 | 0.02–0.05 |
| Combined data set (the present study, [45–47]) | 50 | 226.7 | 4.5 | 0.992 | 85.0 | 4.3 | 0.993 | 233.7 | 6.5 | 0.950 | 0.02–0.60 |

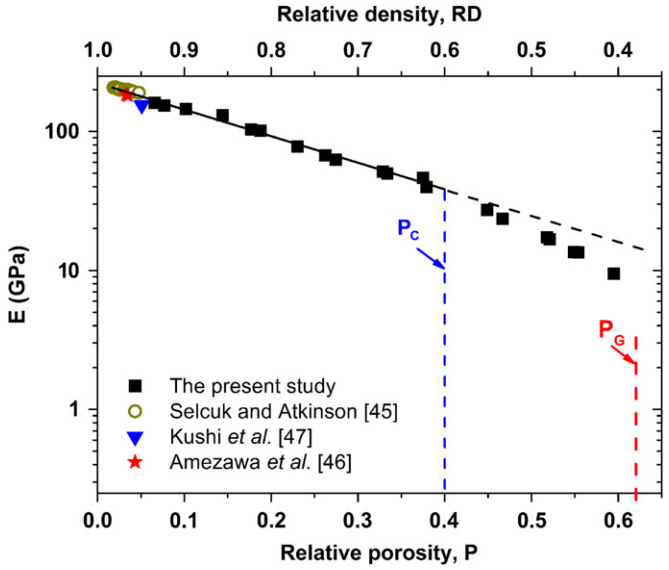


Fig. 5. Semi-log plot of the Young's modulus versus porosity for GDC10 specimens from the combined data set (the present study, Selcuk and Atkinson [45], Amezawa et al. [46], and Kushi et al. [47]). The solid line represents the least-squares fit of $E$–$P$ data with P up to $P_C \sim 0.4$ to Eq. (2), and the dashed line is the extrapolation of the solid line to higher porosity values.

at higher porosity (say, $P > 0.30$ or 0.40) is not as good as the fit at lower $P$ values [50]. For example, Eq. (2) describes well the elastic modulus versus porosity change in ceramics for the porosity range $0 < P < P_c$, where $P_c$ is a critical porosity value [50]. For $P > P_c$, the elastic moduli decrease faster with increasing $P$ than predicted by Eq. (2). According to Rice [50], the value of $P_c$ depends on the pore size and spatial distribution of pores, as well as the state of agglomeration of the powders, size of initial powders, powder packing parameters and fabrication techniques. However, neither Rice [50] nor others in the literature give particular functional relationships for the dependence of $P_c$ on such microstructural or processing parameters. Based on empirical observations, for uniaxially hard die pressed and sintered powders, $P_c \sim 0.5$ for alumina [62] and $P_c \sim 0.5$ for hydroxyapatite [33].

For the GDC10 data in the present study, a semi-log plot of $E$ versus $P$ for the combined data set [the present study, 31–33] (Fig. 5) shows that in a semi-logarithmic plot, the fit to Eq. (2) is excellent for $0 < P < 0.4$, however, beginning at approximately $P = \sim 0.45$, $E$ begins to deviate from the behavior predicted by Eq. (2) such that the Young's modulus drops off faster than the least squares fit to Eq. (2). Thus, this behavior is consistent with that described by Rice [50] for the drop-off in $E$ for $P > P_C$. It is important to note that this disagreement is not the result of a difference in oxygen nonstoichiometry (and hence different lattice parameters and elastic properties [48]) for samples with different porosities/grain sizes. Powder x-ray diffraction (XRD) analyses of specimen ♯5 (with a grain size of 1.1 μm) and the raw GDC powder (with a grain size of ~27 nm) yielded XRD peak positions that were identical within the 0.2° resolution of the XRD; resulting in a lattice parameter of $5.418 \pm 0.011$ A for both samples. The reduced GDC mechanical property study of Wang et al. [48] indicates that the small oxygen vacancy concentration differences indicated by such small lattice parameter differences would not cause observable elastic modulus changes.

### 3.3. Poisson's ratio as a function of P

The porosity dependence of Poisson's ratio, $\nu$, is more complicated than that for $E$, $G$ and $B$. In the literature, $\nu$ is relatively insensitive to $P$ for alumina [63] and LAST (Lead–antimony–silver–tellurium) [64]. However, based on empirical observations Boccaccini [65] suggested that the changes in $\nu$ as a function of $P$ is related to $\nu_0$, the values of Poisson's ratio at $P = 0$ for a given material. For literature from fifteen different ceramics, including both oxides and non-oxides, for $\nu_0 > 0.25$, $\nu$ tended to decrease as $P$ increased and for $\nu_0 < 0.25$, $\nu$ tended to increase as $P$ increased [65].

For the GDC10 specimens in the present study, Poisson's ratio decreased with increasing porosity (Fig. 6). For $P = 0.07$, $\nu$ is approximately 0.29 and for $0.5 < P < 0.6$, $\nu$ dropped to approximately 0.21. Thus, the $\nu$ versus P behavior for GDC10 specimens is broadly consistent with the trends identified by Boccaccini [65]. Also, although Amezawa [46] and Kushi [47] did not report the $\nu$ values, the value of $\nu$ can be computed from Amezawa et al.'s [46] and Kushi et al.'s [47] $E$ and $G$ data via [66]

$$\nu = E/2G - 1 \tag{8}$$

For the combined data (with data from the present study, and references [45–47]), a least-squares fit of Poisson's ratio versus $P$ using both Eq. (3) (linear) and Eq. (2) (exponential) yielded $\nu_0 = 0.33$, with coefficients of determination, $R^2$, of 0.819 and 0.844, respectively. Although the fit to Eqs. (2) and (3) is relatively poor, this is

likely due in part to the inherent scatter in the $\upsilon$ versus $P$ data.

### 3.4. Elastic modulus-porosity for other materials in the literature

The literature also shows that porosity dependence of the Young's modulus-porosity, for example, can be described by Eq. (2) for a number of oxides such as $Al_2O_3$ [33], $Ca_{10}(PO_4)_6(OH)_2$ [33], 3Y–TZP [67], (Bi–Pb)SrCaCuO [68], CoO [69], $Co_{0.5}Mg_{0.5}O$ [69] and $CoAl_2O_4$ [69] (Table 4).

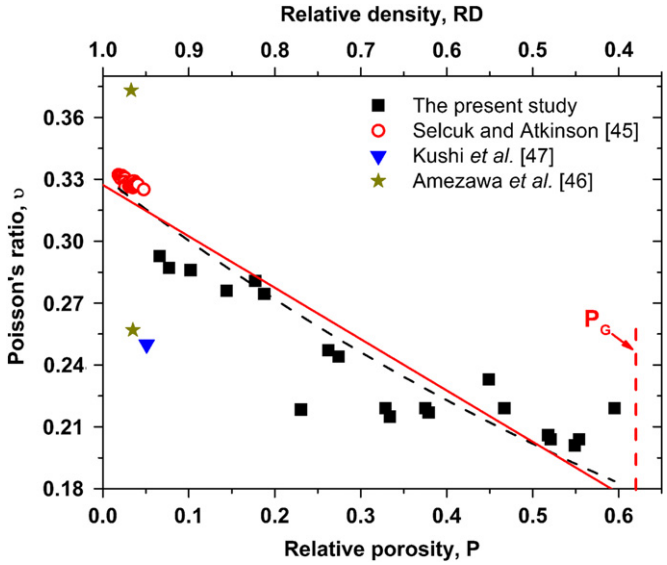


Fig. 6. Poisson's ratio for GDC10 specimens for the combined data set (the present study, Selcuk and Atkinson [45], Amezawa et al. [46], and Kushi et al. [47]). The solid curves represents the least-squares fit of the $\upsilon$–$P$ data to Eq. (3) and the dashed curves represents the least-squares fit of the $\upsilon$–$P$ data to Eq. (2).

In addition, $b_E$ values from the literature for the seven oxides listed in Table 4 bracket the $b_E$ of 4.7 for GDC10 in the present study, namely the $b_E$ ranges from 5.39 for $CoAl_2O_4$ [69] to 2.77 for (Bi–Pb)SrCaCuO [68].

For the GDC10 specimens in the present study, the Young's modulus dropped from $\sim$160 GPa to $\sim$10 GPa as $P$ increased from 0.07 to 0.60. This dramatic drop in elastic modulus with increasing $P$ also is consistent with the literature for a wide range of materials including the oxides $(Ca_{10}(PO_4)_6(OH)_2$ [32], $Al_2O_3$ [62,70], YSZ [71] and metal Ti [72] (Table 5). The degree of densification, $\phi$, ($\phi = 1 - P/P_G$) was included in Table 5 to facilitate direct comparison among studies with differing values of the green porosity, $P_G$ (the present study, [32,43,62,70–72]). If we consider $E_{PNG}$, the Young's modulus at $P \sim P_G$ and normalize $E_{PNG}$ by $E_0$, then $E_{PNG}/E_0$ is roughly 0.04–0.09 for a number of materials, including GDC10 in the present study, as well as $(Ca_{10}(PO_4)_6(OH)_2$ [32], $Al_2O_3$ [62,70], YSZ [71] Ti [72] (Table 5).

## 4. Summary and conclusions

Twenty-one $Ce_{0.9}Gd_{0.1}O_{1.95}$ (GDC10) specimens were hard-die pressed and partially sintered in air at temperatures from 825 °C to 1475 °C for 5 h to produce specimens with volume fraction porosities, $P$, from 0.07 to 0.60. Room temperature Young's, $E$, shear, $G$. and bulk, $B$, moduli were measured as a function of $P$ using resonant ultrasound spectroscopy. The least-squares fit of $E$, $G$. and $B$ to Eqs. (2)–(5) showed that the exponential equation (Eq. (2)) best described the observed porosity dependence. The values of $E_0$, $G_0$ and $B_0$, obtained by extrapolating $E$, $G$ and $B$ to zero porosity are useful since $E_0$, $G_0$ and $B_0$ can be compared to (1) aggregated average moduli from single

Table 4
The values of $b_E$ obtained from a least-squares fit of the Young's modulus, $E$, versus porosity, $P$, data to the Eq. (2) for the GDC10 specimens included in this study and several oxides from the literature. The number of data points, ND, included in the least-squares fit and the relative porosity range of the data is also specified.

| Reference | Material | $b_E$ value | $E$ range (GPa) | $E$ measurement method | Processing technique | Relative porosity range | ND |
|---|---|---|---|---|---|---|---|
| The present study | $Ce_{0.9}Gd_{0.1}O_{1.95}$ | $4.7 \pm 0.2$ | 9.5–158.3 | Resonant ultrasound spectroscopy | Hard die pressed at 27.3 MPa, sintered from 825–1450 °C for 5 h | 0.066–0.595 | 21 |
| Ren et al. [33] | $Ca_{10}(PO_4)_6(OH)_2$ | $3.4 \pm 0.2$ | 12–107 | Resonant ultrasound spectroscopy | Uniaxially cold pressed at 33 MPa, 1125–1360 °C for 1–6 h | 0.05–0.51 | 15 |
| | $Al_2O_3$ | $3.4 \pm 0.1$ | 105–340 | Resonant ultrasound spectroscopy | Uniaxially cold pressed at 23 MPa, 1200–1475 °C for 1–4 h | 0.06–0.39 | 9 |
| Luo and Stevens [67] | 3Y –TZP | 3.69 | 50–220 | Ultrasonic velocity method | Single action die pressing followed by CIP. Sintered at 1150–1450 °C | 0–0.38 | 12 |
| Oduleye et al. [68] | (Bi-Pb)SrCaCuO | 2.77 | 30–75 | Bending test | Extruded. Sintered at 810–855 °C | 0.2–0.53 | 17 |
| Petrak et al. [69] | CoO | 4.51 | 103–159 | Resonant sphere technique | Pressed, sintered at 1400 °C in Ar. Also hot pressed at 1300 °C | 0.09–0.20 | 8 |
| | $Co_{0.5}Mg_{0.5}O$ | 4.36 | 137–206 | Resonant sphere technique | Pressed, sintered at 1650–1700 °C in air | 0.05–0.15 | 8 |
| | $CoAl_2O_4$ | 5.39 | 124–234 | Resonant sphere technique | Pressed, sintered at 1650–1700 °C in air | 0.03–0.15 | 10 |

Table 5
From the literature for the Young's modulus for partially sintered powder compacts including the GDC10 specimens in this study, three oxides and titanium metal, the values of $E_{PNG}/E_0$, where $E_{PNG}$ is the Young's modulus at $P \sim P_G$ and $E_0$ is the Young's modulus at $P=0$. $E_{PNG}/E_0$ is similar for each material, where $E_{PNG}/E_0$ is independent of the choice of $E$ versus $P$ model. The degree of densification, $\phi$, is also given.

| Reference | Material | Porosity | $E$ (GPa) | $E_{PNG}/E_0$ | $E$ measurement method | Processing technique | $\phi$ | Green porosity |
|---|---|---|---|---|---|---|---|---|
| The present study | $Ce_{0.9}Gd_{0.1}O_{1.95}$ | 0.595 | 9.5 | 0.04 | Resonant ultrasound spectroscopy | Hard die pressed at 27.3 MPa, sintered at 825 °C for 5 h | 0.04 | 0.62 |
| Fan et al. [32] | $Ca_{10}(PO_4)_6(OH)_2$ | 0.55 | 8.3 | 0.07 | Resonant ultrasound spectroscopy | Uniaxially cold pressed at 33 MPa, sintered at 550 °C for 2 h | 0.11 | 0.62 |
| Hardy et al. [62] | $Al_2O_3$ | 0.45 | 36 | 0.09 | Ultrasonic velocity technique | Uniaxially pressed at 45 MPa, sintered at 800 °C for 2 h | 0.01 | 0.46 |
| Nanjangud et al. [70] | $Al_2O_3$ | 0.415 | 20 | 0.05 | Ultrasonic velocity technique | Extruded, sintered at 800 °C for 2 h | 0.01 | 0.42 |
| Deng et al. [71] | YSZ | 0.51 | 21 | 0.09 | Pulse-echo method | Single-ended pressing at 75 MPa, sintered at 1100 °C for 30 min | 0.09 | 0.56 |
| Oh et al. [72] | Ti | 0.356 | 9 | 0.08 | Compression test | Pressed at 70 MPa for 0.6 ks, sintered at 1573 K for 7.2 ks | 0.01 | 0.36 |

crystal data or (2) elastic moduli calculated from density functional theory.

The decrease in elastic moduli with increasing $P$ was very dramatic, with the $E$, $G$ and $B$ values at $P=0.60$ being only on the order of roughly 5% of the $E_0$, $G_0$ and $B_0$ values, respectively. As summarized in Table 5, for specimens with very high porosity levels, similar drastic decreases in elastic moduli for specimens have been observed for a number of other oxide materials in addition to GDC10.

In solid oxide fuel cell applications, porous GDC structure will undergo thermal and mechanical stresses arising from manufacturing, external loading and differences in thermal expansion coefficients between cell layers. The knowledge of elastic moduli of GDC is essential to model the response of SOFCs to internal or external stresses and to design more reliable SOFCs with longer service life. Thus, it is of great importance to know the elastic moduli at different porosity levels since without using the appropriate moduli in analytical and numerical models, the predicted stresses and strains will exhibit very large errors.

## Acknowledgments

This work was supported, in part, through a Michigan State University Faculty Startup Package.

## References

[1] B.C.H. Steele, A. Heinzel, Materials for fuel–cell technologies, Nature 414 (2001) 345–352.
[2] J.W. Fergus, Electrolytes for solid oxide fuel cells, Journal of Power Sources 162 (2006) 30–40.
[3] H.J.M. Bouwmeester, A.J. Burggraff, Dense ceramic membranes for oxygen separation, in: P.J. Gellings, H.J.M. Bouwmeester (Eds.), The CRC Handbook of Solid State Electrochemistry, CRC Press, New York, 1997, pp. 481–554.
[4] A.L. Sauvet, J. Fouletier, Catalytic properties of new anode materials for solid oxide fuel cells operated under methane at intermediary temperature, Journal of Power Sources 101 (2001) 259–266.
[5] A. Trovarelli, Catalytic properties of ceria and $CeO_2$-containing materials, Catalysis Reviews: Science and Engineering 38 (1996) 439–509.
[6] J.B. Goodenough, Y.-H. Huang, Alternative anode materials for solid oxide fuel cells, Journal of Power Sources 173 (1) (2007) 1–10.
[7] J. Liu, B.D. Madsen, Z. Ji, S.A. Barnett, A fuel-flexible ceramic-based anode for solid oxide fuel cells, Electrochemical and Solid-State Letters 5 (6) (2002) A122–A124.
[8] E.P. Murray, S.A. Barnett, (La,Sr)MnO3–(Ce,Gd)O(2−$x$) composite cathodes for solid oxide fuel cells, Solid State Ionics 143 (2001) 265–273.
[9] J.D. Nicholas, L. Wang, A.V. Call, S.A. Barnett, Use of the simple infiltration microstructure polarization loss estimation (SIMPLE) model to predict the measured polarization resistance of infiltrated nano-composite solid oxide fuel cell cathodes, Physical Chemistry Chemical Physics 14 (2012) 15379–15392.
[10] J.D. Nicholas, S.A. Barnett, Measurements and modeling of $Sm_{0.5}Sr_{0.5}CoO_{3-x}$—$Ce_{0.9}Gd_{0.1}O_{1.95}$ SOFC cathodes produced using infiltrate solution additives, Journal of the Electrochemical Society 157 (2010) B536–B541.
[11] M. Shah, J.D. Nicholas, S.A. Barnett, Prediction of infiltrated solid oxide fuel cell cathode polarization resistance using simple models, Electrochemistry Communications 11 (2009) 2–5.
[12] M. Shah, S.A. Barnett, Solid oxide fuel cell cathodes by infiltration of $La_{0.6}Sr_{0.4}Co_{0.2}Fe_{0.8}O_{3-x}$ into Gd-doped ceria, Solid State Ionics 179 (2008) 2059–2064.
[13] A. Samson, M. Sogaard, R. Knibbe, N. Bonanos, High performance cathodes for solid oxide fuel cells prepared by infiltration of $La_{0.6}Sr_{0.4}CoO_{3-\delta}$ into Gd-doped ceria, Journal of the Electrochemical Society 158 (6) (2011) B650–B659.
[14] A.J. Samson, P. Hjalmarsson, M. Søgaard, J. Hjelm, N. Bonanos, Highly durable anode supported solid oxide fuel cell with an infiltrated cathode, Journal of Power Sources 216 (0) (2012) 124–130.
[15] S.P. Jiang, A review of wet impregnation—an alternative method for the fabrication of high performance and nano-structured electrodes of solid oxide fuel cells, Materials Science and Engineering A: Structural Materials, Properties, Microstructure and Processing 418 (1–2) (2006) 199–210.
[16] J.M. Vohs, R.J. Gorte, High-performance SOFC cathodes prepared by infiltration, Advanced Materials 21 (9) (2009) 943–956.
[17] B. Sun, R.A. Rudkin, A. Atkinson, Effect of thermal cycling on residual stress and curvature of anode-supported SOFCs, Fuel Cells 9 (6) (2009) 805–813.
[18] C.K. Lin, T.T. Chen, Y.P. Chyou, L.K. Chiang, Thermal stress analysis of a planar SOFC stack, Journal of Power Sources 164 (1) (2007) 238–251.

[19] C.S. Montross, H. Yokokawa, M. Dokiya, Thermal stresses in planar solid oxide fuel cells due to thermal expansion differences, British Ceramic Transactions 101 (3) (2002) 85–93.
[20] J.E. Shemilt, H.M. Williams, M.J. Edirsinghe, J.R.G. Evans, B. Ralph, Fracture toughness of doped-ceria ceramics, Scripta Materialia 36 (1997) 929–934.
[21] Y.P. Fu, S.H. Chen, J.J. Huang, Preparation and characterization of $Ce_{0.8}M_{0.2}O_{2-\delta}$ (M=Y, Gd, Sm, Nd, La) solid electrolyte materials for solid oxide fuel cells, International Journal of Hydrogen Energy 35 (2) (2010) 745–752.
[22] M. Morales, J.J. Roa, X.G. Capdevila, M. Segarra, S. Pinol, Mechanical properties at the nanometer scale of GDC and YSZ used as electrolytes for solid oxide fuel cells, Acta Materialia 58 (7) (2010) 2504–2509.
[23] T. Ishida, F. Iguchi, K. Sato, T. Hashida, H. Yugami, Fracture properties of $(CeO_2)_{1-x}(RO_{1.5})_x$ (R=Y, Gd, and Sm; $x=0.02-0.20$) ceramics, Solid State Ionics 176 (31–34) (2005) 2417–2421.
[24] K.R. Reddy, K. Karan, Sinterability, mechanical, microstructural, and electrical properties of gadolinium-doped ceria electrolyte for low-temperature solid oxide fuel cells, Journal of Electroceramics 15 (1) (2005) 45–56.
[25] Y. Ikuma, T. Uchida, High temperature creep of stoichiometric polycrystalline $CeO_2$ at low stresses, Journal of Materials Science 16 (20) (1997) 1637–1639.
[26] A. Nakajo, J. Kuebler, A. Faes, U.F. Vogt, H.J. Schindler, L.-K. Chiang, S. Modena, J. Van herle, T. Hocker, Compilation of mechanical properties for the structural analysis of solid oxide fuel cell stacks. Constitutive materials of anode-supported cells, Ceramics International 38 (5) (2012) 3907–3927.
[27] A. Nakajo, F. Mueller, J. Brouwer, J. Van Herle, D. Favrat, Mechanical reliability and durability of SOFC stacks. Part II: modelling of mechanical failures during ageing and cycling, International Journal of Hydrogen Energy 37 (11) (2012) 9269–9286.
[28] J.L. Routbort, K.C. Goretta, A.R. de Arellano-López, J. Wolfenstine, Creep of $Ce_{0.9}Gd_{0.1}O_{1.95}$, Scripta Materialia 38 (2) (1997) 315–320.
[29] J.D. Nicholas, L.C. DeJonghe, Prediction and evaluation of sintering aids for cerium gadolinium oxide, Solid State Ionics 178 (19–20) (2007) 1187–1194.
[30] A. Migliori, J.D. Maynard, Implementation of a modern resonant ultrasound spectroscopy system for the measurement of the elastic moduli of small solid specimens, Review of Scientific Instruments 76 (12) (2005).
[31] A. Migliori, J.L. Sarrao, W.M. Visscher, T.M. Bell, M. Lei, Z. Fisk, R.G. Leisure, Resonant ultrasound spectroscopic techniques for measurement of the elastic moduli of solids, Physica B 183 (1–2) (1993) 1–24.
[32] X. Fan, E.D. Case, F. Ren, Y. Shu, M.J. Baumann, Part II: fracture strength and elastic modulus as a function of porosity for hydroxyapatite and other brittle materials, Journal of the Mechanical Behavior of Biomedical Materials 8 (2012) 99–110.
[33] F. Ren, E.D. Case, A. Morrison, M. Tafesse, M.J. Baumann, Resonant ultrasound spectroscopy measurement of Young's modulus, shear modulus and Poisson's ratio as a function of porosity for alumina and hydroxyapatite, Philosophical Magazine 89 (14) (2009) 1163–1182.
[34] J.E. Ni, E.D. Case, J.S. Sakamoto, J.B. Wolfenstein, Room temperature elastic moduli and vickers hardness of hot-pressed LLZO cubic garnet, Journal of Materials Science 47 (2012) 7978–7985.
[35] H. Seiner, P. Sedlak, L. Bodnarova, A. Kruisova, M. Landa, A. de Pablos, M. Belmonte, Sensitivity of the resonant ultrasound spectroscopy to weak gradients of elastic properties, Journal of the Acoustical Society of America 131 (5) (2012) 3775–3785.
[36] A.Q. Morrison, E.D. Case, F. Ren, A.J. Baumann, D.C. Kleinow, J.E. Ni, T.P. Hogan, J. D'Angelo, N.A. Matchanov, T.J. Hendricks, N.K. Karri, C. Cauchy, J. Barnard, M.G. Kanatzidis, Elastic modulus, biaxial fracture strength, electrical and thermal transport properties of thermally fatigued hot pressed LAST and LASTT thermoelectric materials, Materials Chemistry and Physics 134 (2-3) (2012) 973–987.
[37] R.D. Schmidt, E.D. Case, J. Giles III, J.E. Ni, T.P. Hogan, Room-temperature mechanical properties and slow crack growth behavior of $Mg_2Si$ thermoelectric materials, Journal of Electronic Materials 41 (6) (2012) 1210–1216.
[38] D.H. Hurley, S.J. Reese, S.K. Park, Z. Utegulov, J.R. Kennedy, K.L. Telschow, In situ laser-based resonant ultrasound measurements of microstructure mediated mechanical property evolution, Journal of Applied Physics 107 (6) (2010).
[39] G. Kaplan, T.W. Darling, K.R. McCall, Resonant ultrasound spectroscopy and homogeneity in polycrystals, Ultrasonics 49 (1) (2009) 139–142.
[40] S. Gorsse, D.B. Miracle, Mechanical properties of Ti–6Al–4V/TiB composites with randomly oriented and aligned TiB reinforcements, Acta Materialia 51 (9) (2003) 2427–2442.
[41] O.V. Vdovychenko, V.S. Voropaev, A.N. Slipenyuk, Effect of microstructure on Young's modulus of extruded Al–SiC composites studied by resonant ultrasound spectroscopy, Journal of Materials Science 41 (24) (2006) 8329–8338.
[42] E.E. Underwood, A.R. Colcord, R.C. Waugh, Quantitative relationships for random microstructures, in: R.M. Fulrath, J.A. Pask (Eds.), Ceramic Microstructures, John Wiley & Sons, New York, 1968, p. 25.
[43] X. Fan, E.D. Case, F. Ren, Y. Shu, M.J. Baumann, Part I: porosity dependence of the weibull modulus for hydroxyapatite and other brittle materials, Journal of the Mechanical Behavior of Biomedical Materials 8 (2012) 21–36.
[44] K.A. Berry, M.P. Harmer, Effect of MgO solute on microstructure development in $Al_2O_3$, Journal of the American Ceramic Society 69 (2) (1986) 143–149.
[45] A. Selcuk, A. Atkinson, Elastic properties of ceramic oxides used in solid oxide fuel cells, Journal of the European Ceramic Society 17 (1997) 1523–1532.
[46] K. Amezawa, T. Kushi, K. Sato, A. Unemoto, S.-i. Hashimoto, T. Kawada, Elastic moduli of $Ce_{0.9}Gd_{0.1}O_{2-\delta}$ at high temperatures under controlled atmospheres, Solid State Ionics 198 (1) (2011) 32–38.
[47] T. Kushi, K. Sato, A. Unemoto, K. Amezawa, T. Kawada, Investigation of high tempearture elastic modulus and internal friction of SOFC electrolytes using resonance method, Electrochemical Society Transactions 25 (2) (2009) 1673–1677.
[48] Y. Wang, K. Duncan, E.D. Wachsman, F. Ebrahimi, The effect of oxygen vacancy concentration on the elastic modulus of fluorite-structured oxides, Solid State Ionics 178 (1–2) (2007) 53–58.
[49] E. Wachtel, I. Lubomirsky, The elastic modulus of pure and doped ceria, Scripta Materialia 65 (2) (2011) 112–117.
[50] R.W. Rice, Porosity of Ceramics, Marcel Dekker, New York, 1998.
[51] D.P.H. Hasselman, On the porosity dependence of the elastic moduli of polycrystalline refractory materials, Journal of the American Ceramic Society 45 (9) (1962) 452–453.
[52] N. Ramakrishnan, V.S. Arunachalam, Effective elastic moduli of porous ceramic materials, Journal of the American Ceramic Society 76 (11) (1993) 2745–2752.
[53] G. Simmons, H. Wang, Single Crystal Elastic Constants and Calculated Aggregate Properties: A Handbook, MIT Press, Cambridge, MA, 1971.
[54] V. Kanchana, G. Vaitheeswaran, A. Svane, A. Delin, First-principles study of elastic properties of $CeO_2$, $ThO_2$ and $PoO_2$, Journal of Physics: Condensed Matter 18 (42) (2006) 9615–9624.
[55] V. Van Hung, L.T. Mai Thanh, Study of elastic properties of $CeO_2$ by statistical moment method, Physica B 406 (21) (2011) 4014–4018.
[56] T. Hashida, K. Sato, Y. Takeyama, T. Kawada, J. Mizusaki, Deformation and fracture characteristics of zirconia and ceria-based electrolytes for SOFCs under reducing atmospheres, Electrochemical Society Transactions 25 (2) (2009) 1565–1575.
[57] X. Huang, Q. Yang, Effects of co-doping on elastic modulus for zirconia based ternary ceramic materials, Materials Science and Technology 24 (6) (2008) 751–755.

[58] K.L. Duncan, Y.L. Wang, S.R. Bishop, F. Ebrahimi, E.D. Wachsman, The role of point defects in the physical properties of nonstoichiometric ceria, Journal of Applied Physics 101 (4) (2007).
[59] W.C. Oliver, G.M. Pharr, An improved technique for determining hardness and elastic modulus using load and displacement sensing indentation experiments, Journal of Materials Research 7 (6) (1992) 1564–1583.
[60] M. Radovic, E. Lara-Curzio, L. Riester, Comparison of different experimental techniques for determination of elastic properties of solids, Materials Science and Engineering A: Structural Materials Properties Microstructure and Processing 368 (1–2) (2004) 56–70.
[61] R.D. Schmidt, J.E. Ni, E.D. Case, J.S. Sakamoto, D.C. Kleinow, B.L. Wing, R.C. Stewart, E.J. Timm, Room temperature Young's modulus, shear modulus, and Poisson's ratio of $Ce_{0.9}Fe_{3.5}Co_{0.5}Sb_{12}$ and $Co_{0.95}Pd_{0.05}Te_{0.05}Sb_3$ skutterudite materials, Journal of Alloys and Compounds 504 (2) (2010) 303–309.
[62] D. Hardy, D.J. Green, Mechanical properties of partially sintered alumina, Journal of the European Ceramic Society 15 (8) (1995) 769–775.
[63] K.K. Phani, A. Novel, Method of predicting ultrasonic and elastic properties of isotropic ceramic materials after sintering from the properties of partially sintered or green compacts, Journal of the American Ceramic Society 91 (1) (2008) 215–222.
[64] J.E. Ni, F. Ren, E.D. Case, E.J. Timm, Porosity dependence of elastic moduli in LAST (lead–antimony–silver–tellurium) thermoelectric materials, Materials Chemistry and Physics 118 (2–3) (2009) 459–466.
[65] A.R. Boccaccini, Effective elastic moduli of porous ceramic materials-comment, Journal of the American Ceramic Society 77 (10) (1994) 2779–2781.
[66] J.B. Wachtman, W.R. Cannon, M.J. Matthewson, Mechanical Properties of Ceramics, John Wiley & Sons, New York, 2009.
[67] J. Luo, R. Stevens, Porosity dependence of elastic moduli and hardness of 3Y–TZP ceramics, Ceramics International 25 (3) (1999) 281–286.
[68] O.O. Oduleye, S.J. Penn, N.M. Alford, The mechanical properties of (Bi–Pb)SrCaCuO, Superconductor Science and Technology 11 (9) (1998) 858–865.
[69] D.R. Petrak, D.T. Rankin, R. Ruh, R.D. Sisson, Effect of porosity on elastic moduli of CoO, CoO–MgO solid solutions, and $CoAl_2O_4$, Journal of the American Ceramic Society 58 (1–2) (1975) 78–79.
[70] S.C. Nanjangud, R. Brezny, D.J. Green, Strength and Youngs modulus behavior of a partially sintered porous alumina, Journal of the American Ceramic Society 78 (1) (1995) 266–268.
[71] Z.Y. Deng, J.F. Yang, Y. Beppu, M. Ando, T. Ohji, Effect of agglomeration on mechanical properties of porous zirconia fabricated by partial sintering, Journal of the American Ceramic Society 85 (8) (2002) 1961–1965.
[72] I.H. Oh, N. Nomura, N. Masahashi, S. Hanada, Mechanical properties of porous titanium compacts prepared by powder sintering, Scripta Materialia 49 (12) (2003) 1197–1202.